



# Phase transformation behavior in titanium single-crystal nanopillars under [0001] orientation tension: A molecular dynamics simulation



Junqiang Ren, Qiaoyan Sun, Lin Xiao\*, Xiangdong Ding, Jun Sun

State Key Laboratory for Mechanical Behaviour of Materials, Xi'an Jiaotong University, Xi'an, Shaanxi 710049, PR China

## ARTICLE INFO

### Article history:

Received 14 February 2014

Received in revised form 10 May 2014

Accepted 13 May 2014

### Keywords:

Molecular dynamics

Titanium

Dislocations

Twinning

Phase transformations

## ABSTRACT

Molecular dynamics simulations reveal a rare phase transformation from the hexagonal close-packed (hcp) phase to the face-centered cubic (fcc) phase inside the  $\{10\bar{1}2\}(10\bar{1}1)$  twinning region in high-purity  $\alpha$ -titanium (Ti) single-crystal nanopillars orientated along [0001] during tension. This unique hcp to fcc phase transformation is induced by dislocation glide of multiple Shockley partial dislocations under the condition of size restriction.

© 2014 Elsevier B.V. All rights reserved.

## 1. Introduction

Ti and its alloys have a wide range of applications such as in aerospace sector, chemical industry, medical engineering, and leisure sector due to their high specific strength and excellent corrosion resistance. Recently, Ti and its alloys have been proposed as a suitable semiconductor-based micro-electromechanical systems (MEMS) [1] and MEMS-based wing technology [2] for its brilliant electrical and mechanical properties. The use of Ti and its alloys at nano- and microscale in emerging technologies demands a thorough understanding of their structures and properties. Ti and its majority alloys exhibit a hexagonal close-packed (hcp) crystal structure at low temperatures, called  $\alpha$ -Ti, and the body-centered cubic structure is stable at high temperatures ( $>882 \pm 2^\circ\text{C}$ ), which is referred to as  $\beta$ -Ti [3]. The face-centered cubic (fcc) crystal structure does not exist on the conventional pressure–temperature phase diagrams of Ti [4–18]. However, Hong et al. recently reported a stress-induced transformation from the hcp-Ti phase to the fcc-Ti phase [7]. Experimental observations showed an epitaxial growth of fcc-Ti thin films on metallic and semiconductor substrates [7–13]. Fcc-Ti was also reported in Ti/Ni and Ti/Al epitaxial multilayer films [8,9]. A metastable fcc-Ti phase was observed in bulk Ti powders during mechanical milling [14–16] and in heat-treated Ti alloys [17–19]. Additionally, the first-principle calculations by Sliwko et al. [20] and Aguayo et al. [21]

demonstrated that fcc-Ti has a minimum total energy and has a local stable structure.

The loading mode has an important effect on the plastic deformation behavior of hcp-Ti at the submicron scale and nanoscale [22–29]. Yu et al. [22] reported that the plastic deformation behavior of single crystalline Ti-5 at. % Al nano- and micropillars under uniaxial compression is dependent on the size of the pillars. The authors observed an increase in stress for twinning in the smaller pillars, including a transition in the deformation mechanism from twinning to dislocation slip when the sample size was reduced to below approximately  $1\ \mu\text{m}$ . More recently, they observed different types of  $\{10\bar{1}2\}$  twinning in hcp magnesium (Mg) single-crystal nanopillars under tension but  $\{10\bar{1}1\}$  twinning under compression [23]. Ye et al. [24], through in situ transmission electron microscopy (TEM) nanocompression testing, suggested that the size effect is associated with basal slip and extended twins in Mg and its alloys. In their experiments, the twin boundary was observed to migrate until most of the pillars was converted to the twinned orientation. Microcompression experiments of Mg single crystals along the  $c$ -axis [0001] did not lead to twinning and showed little size effect of strength in the range of  $2.5\text{--}10\ \mu\text{m}$  [25] and  $2.1\text{--}10\ \mu\text{m}$  [26]. Pyramidal slip was the primary deformation mode in these experiments. Compression normal to the  $(11\bar{2}0)$  plane induces non-basal slip and tensile twinning in the early stage of deformation [27]. Uniaxial compression tests revealed that the mechanical strength of cadmium [28] and Ti [29] is sensitive to the size of the specimens. Under nanometer-scale, Molecular dynamics (MD) simulation has

\* Corresponding author. Tel.: +86 29 82668614; fax: +86 29 82663453.

E-mail address: [lxiao@mail.xjtu.edu.cn](mailto:lxiao@mail.xjtu.edu.cn) (L. Xiao).

become an invaluable technique to study the deformation behavior of metallic crystals. The MD can be used to build direct observation the deformation process based on the data at atomic level. In comparison with the experiments, the MD simulation of Ti and other hcp metals nanopillars has attracted limited research attention [30,31]. The primary yielding behavior under uniaxial compression [11 $\bar{2}$ 0]-orientated nanopillars is controlled by double prismatic slips [30]. The {10 $\bar{1}$ 2} twin was found to be the main deformation mechanism under the *c*-axis tension in the Mg single-crystal [31]. These experimental and simulation results provide us with the motivation to study the twinning and phase transformation behavior in Ti single crystals under the severely restrictive condition of specimen size using molecular dynamics (MD) simulations to obtain a better understanding of the twinning and phase transformation mechanisms of hcp single-crystalline Ti nanopillars under tension along the [0001] orientation.

## 2. Simulation methods

MD simulations were run with the software LAMMPS [32] using a many-body potential of the Finnis–Sinclair type, which reproduces relatively good thermo-mechanical properties of the above described Ti, such as the cohesive energy, elastic constants, and surface energies [33]. In MD simulations with the Finnis–Sinclair type of many-body potential, the basic equation for the energy of an atom can be expressed by

$$E_i = \frac{1}{2} \sum_j V(r_{ij}) - \rho_i^{1/2}, \quad \rho_i = \sum_j \phi(r_{ij}) \quad (1)$$

where  $V$  is a pairwise function between neighboring atoms  $i$  and  $j$ ,  $\phi$  is the electronic density function, and  $r_{ij}$  is the distance between atom  $i$  and one of neighboring atoms  $j$ . More detailed parameters are given by Ackland [33].

We focus on the [0001] orientation of a single crystalline Ti nanopillar with dimensions of  $22 \times 11 \times 11 \text{ nm}^3$ . The simulation model included up to 159,236 atoms. The initial pillar structures consisted of a [0001]-oriented single-crystal with a square cross-section. To obtain an equilibrium state before loading, the structure was initially relaxed using the conjugate gradient algorithm. The system energy was minimized by iteratively adjusting the atom coordinates. Then, an additional annealing under zero load was performed for 300 ps at a temperature of 300 K using the Nose–Hoover thermostat [34,35]. The canonical ensemble, i.e., constant atom number, volume, and temperature (NVT), was applied to keep the system temperature at a constant 300 K. The nanopillars were deformed under compression and tension along the loading direction at an engineering strain rate of  $1 \times 10^8 \text{ s}^{-1}$ . All directions were maintained with free boundary conditions. The time step was 1 fs. The snapshots of the MD results were processed with ATOMEYE [36]. The stress calculation in the loading direction is described elsewhere [37].

## 3. Results and discussion

The typical stress–strain curve for the nanopillars subjected to uniaxial tensile loading at 300 K is shown in Fig. 1. The incipient yield points are defined as yield stress. Under tension, nanopillars elastically deform up to the yield stress, which is characterized by a sharp drop in the stress of the stress–strain curve. For the tensile loading, the elastic strain is 0.041. The yield stress for the Ti nanopillar is 4.65 GPa. The second yield point is observed at a strain of 0.12 and the corresponding stress is 3.5 GPa. Beyond the strain of 0.2, further loading causes an extensive plateau with a constant stress of approximately 1.0 GPa.

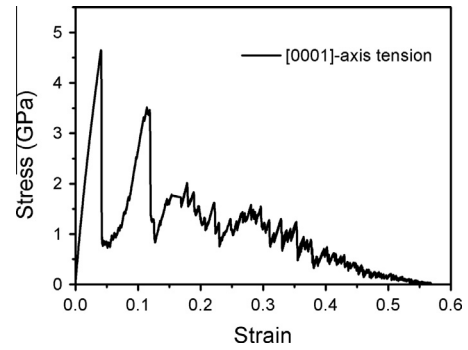


Fig. 1. Typical stress–strain curves of Ti nanopillars subjected to uniaxial tension at 300 K.

The {10 $\bar{1}$ 2} “extension” twin is favored under tension. Fig. 2 illustrates the evolution of the twin under tensile loading. The nucleation of the {10 $\bar{1}$ 2}⟨10 $\bar{1}$ 1⟩ twin resulted in a sudden drop in load at a strain of 4.1%, as shown in Fig. 1. The initial interfaces consist of (0001)<sub>M</sub>||( $\bar{1}$ 100)<sub>T</sub> and ( $\bar{1}$ 100)<sub>M</sub>||( $\bar{1}$ 001)<sub>T</sub> when the nucleus is small and embedded in the matrix. After the nucleation, the twin grows towards the ends of the pillar at a constant stress of approximately 1.0 GPa. The atoms are colored according to common neighbor analysis (CNA) [38]. The hcp atoms are colored light blue, the fcc atoms are colored dark blue, and the defect and surface atoms are colored red. To allow views of the inner defects, the front surface is not shown. According to the analysis of the corresponding atomic configurations during loading, twinning is the underlying mechanism responsible for the tension strain. Twins are nucleated at the yield point in the tension stress–strain curve. As the strain increases, the twin boundaries further propagate toward the ends of the pillars, and the whole pillar transforms from the initial orientation to the new configuration.

To study the influence of the loading condition on the deformation mechanism, compressive loading was also studied. In this case, compression twins and phase transformations were not observed during loading. The pyramidal  $\langle a + c \rangle$  slip dominates plastic deformation at the nanoscale. As deformation proceeds, the Shockley partial dislocations  $b_1$  and  $b_2$  nucleate at the twin boundary (Fig. 2(b)). In particular, the partial dislocations with the same Burgers vector are often generated on atomically adjacent parallel planes where the shear deformation generated the steps on the twin boundary. These partial dislocations glide along the (0001) plane of the matrix following the stacking faults, which are marked by white arrows in Fig. 2(b–c). The final configuration of the well-developed twin is formed, as shown in Fig. 2(d). As a result of the partial crystal being twinned, two twin/matrix interfaces are created, as indicated by a white rectangle in Fig. 2(c). The twinning planes are identified as (10 $\bar{1}$ 2). The twin boundary and accompanying stacking fault are highlighted with a white dashed line in Fig. 2(d). The basal planes of the matrix and of the twin are marked with red lines. During tension, the ( $\bar{1}$ 100) prismatic plane in the twin becomes parallel to the basal plane in the matrix.

As the plastic deformation progressed, the twin boundary migrated through almost the entire pillar, leading to a conversion to the twinned orientation. Stress reduction at the strain of 12% is attributed to the nucleation of new Shockley partial dislocations with a Burgers vector of  $a/6$  [11 $\bar{2}$ 0] from the twin surface of the nanopillar, as shown in Fig. 3(a). Under continuous tensile loading, the deformation of the nanopillar is primarily controlled by the partial dislocations, as marked by the symbol “ $\perp$ ” in Fig. 3(d). The continuous accumulation of a high density of deformation faults was caused by the dislocation glide of multiple Shockley partial dislocations, eventually leading to the allotropic phase



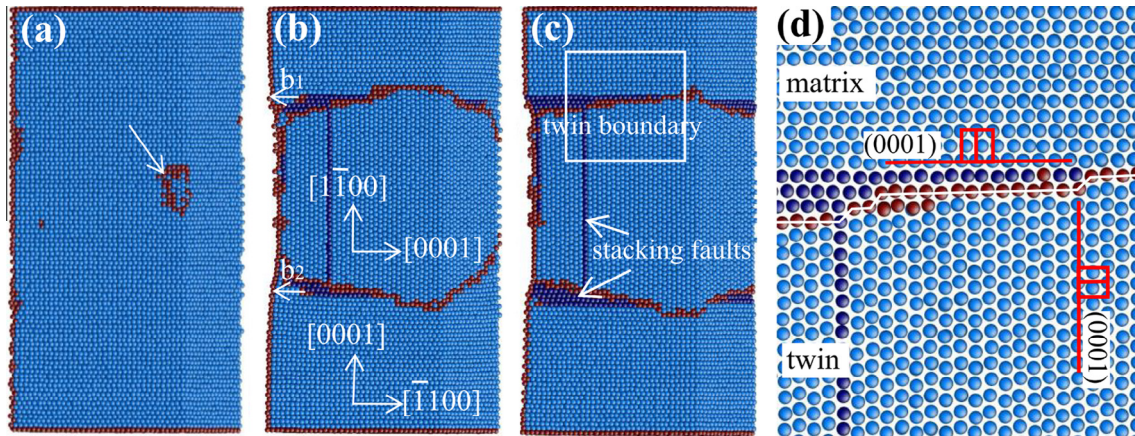


**Fig. 2.** View along the  $[1\bar{1}20]$  direction on the pillar. (a) Tensile twin embryos nucleate at the edges between the  $\{10\bar{1}0\}$  and  $\{\bar{1}2\bar{1}0\}$  surfaces. (b) Partial dislocations are nucleated at the twin boundary and follow the stacking faults. (c) Two interfaces and stacking faults are marked. (d) A blow-up of the atomic configuration at the  $(10\bar{1}2)$  twin boundary.

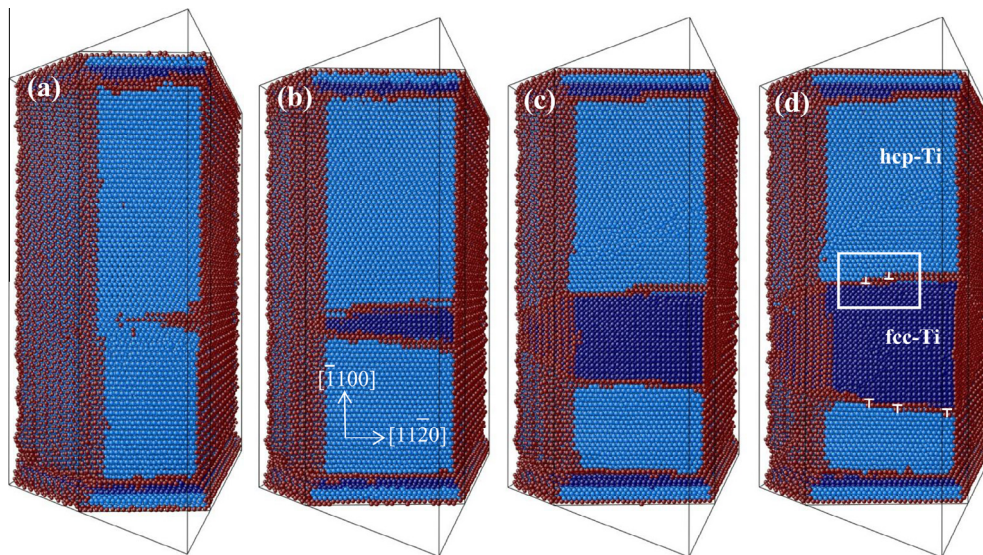


**Fig. 3.** A transformation from a hexagonal close-packed (hcp) phase to a face-centered cubic (fcc) phase in the  $\{10\bar{1}2\}$  twin.

transformation from hcp to fcc [39]. The hcp-Ti to fcc-Ti transformation process is illustrated in Fig. 3.

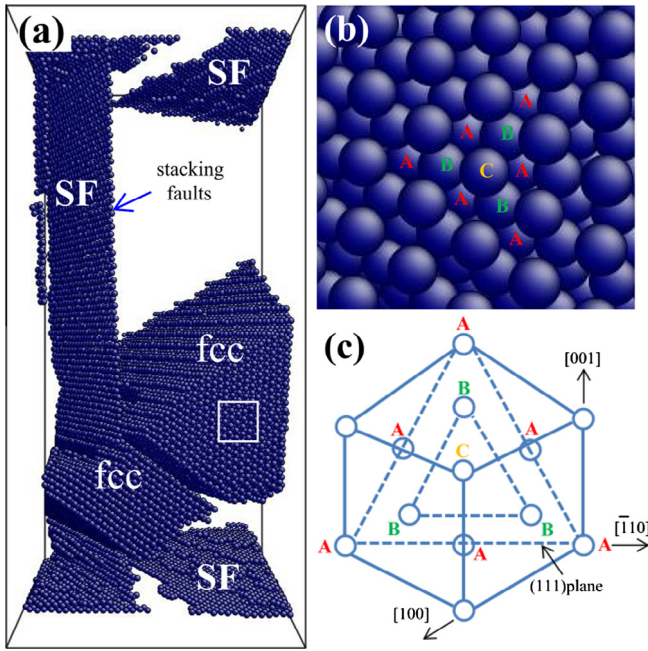
In order to confirm the existence of fcc-Ti in the deformed nanopillar at a strain of 16%, atoms in hcp arrangement and non-coordinated atoms such as atoms near vacancies and free surfaces are not shown in Fig. 4(a) for clarity. The intrinsic stacking fault (ABABACAC...) in hcp phase is marked by a blue arrow in Fig. 4(a). The region enclosed by a white rectangle is magnified and shown in Fig. 4(b). Fig. 4(c) depicts the unit cell of fcc structure and crystallographic orientation. The stacking sequence of  $\{100\}$  plane is ABABAB... and the stacking sequence of  $\{111\}$  plane is ABCABC... The atoms in the  $\{111\}$  planes are in the most close-packed arrangement possible for spheres and contain three  $\langle 110 \rangle$  close-packed directions  $60^\circ$  apart. It reveals that the crystal structure and stacking sequence of atoms of Fig. 4(b) is consistent with that of Fig. 4(c). This convincingly demonstrates that fcc-Ti in the twinning region can be formed under tensile loading.

Fig. 5(a) shows the local structure in detail, which is enclosed by a white rectangle in Fig. 3(d). This figure clearly shows that the fcc phase grew from the phase boundary. The partial dislocations slide along the  $\{10\bar{1}0\}$  plane, as illustrated in Fig. 5(b). The crystallographic analysis reveals that the hcp to fcc phase transformation

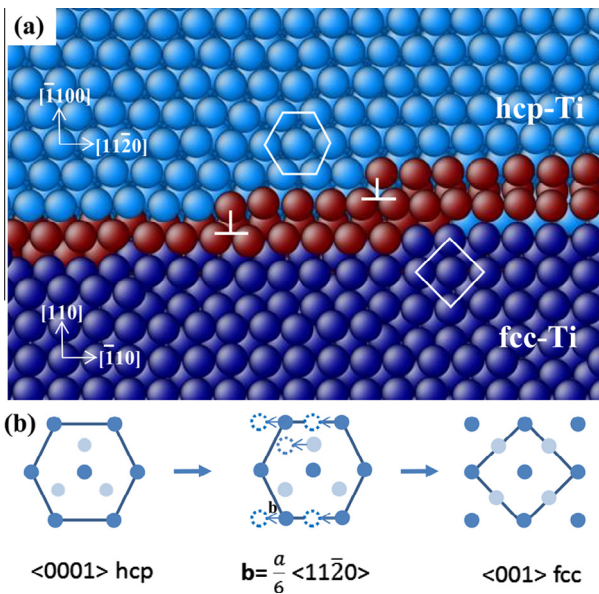
produces orientation relationships of  $\langle 0001 \rangle_{\text{hcp}} \parallel \langle 100 \rangle_{\text{fcc}}$ ,  $\langle 01\bar{1}0 \rangle_{\text{hcp}} \parallel \langle 0\bar{1}1 \rangle_{\text{fcc}}$  and  $\langle 2\bar{1}\bar{1}0 \rangle_{\text{hcp}} \parallel \langle 011 \rangle_{\text{fcc}}$ . A similar transformation was also experimentally observed in pure Ti deformed by cryogenic channel-die compression indented during microstructural refinement [4].

Fig. 6 displays the time evolution of the fraction of each phase in the system. Fcc atoms were not observed in the elastic stage at 0–40 ps. After approximately 40 ps, a small number of fcc atoms in a stacking fault appeared, as shown in the snapshots of Fig. 2. As the plastic deformation progressed, the Shockley partial dislocation with Burgers vector  $b = a/6\langle 1120 \rangle$  movement was observed in the twinning region. At approximately 120 ps, the fraction of fcc atoms quickly increased. The fcc phase reached its maximum fraction, approximately 27% of the system, at a strain of 17.5%. During this time, the fraction of hcp atoms decreased in the twinning region. During the transition, the Shockley partial dislocation with Burgers vector  $b = a/6\langle 112 \rangle$  nucleated and multiplied in the fcc phase under tensile loading. This induced the hcp-type stacking faults in the fcc phase, causing a partial transformation from the fcc phase back to the hcp phase, which inhibited the hcp to fcc phase transformation. The interface between the fcc and hcp phases remained immobile during the inhibition period. At the





**Fig. 4.** (a) Three-dimensional view of the fcc phases and stacking faults in the nanopillar. (b) A close-up of the region enclosed by a rectangle in (a). The stacking sequence of {111} plane are marked by letters A, B and C. (c) The unit cell of fcc structure.



**Fig. 5.** (a) A close-up of the region enclosed by the rectangle in Fig. 3(d). The hcp configuration transforms to the fcc configuration in the middle section of the pillar with an axis along [0001] in the twin. The white hexagon on the upper side shows an hcp unit cell. The white square on the lower side shows fcc lattice cells in the transforming fcc phase. (b) Schematic illustration of direct phase formation from the hcp phase to the fcc phase with the combination of partial dislocations and lattice distortion.

end of the simulation, the fcc phase in the pillar is less than 27%. The fraction of unidentified atom amounts is approximately 10%. These unidentified atoms are situated at the surface of the pillar and at the ragged boundaries between the hcp and fcc phases.

The  $\{10\bar{1}2\} \langle 10\bar{1}1 \rangle$  twinning mode has been commonly observed in many hcp metals. In the current study, the rare hcp to fcc phase transformation occurred when the  $\{10\bar{1}2\} \langle 10\bar{1}1 \rangle$

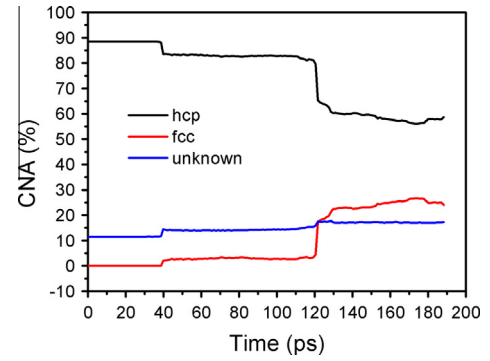


**Fig. 6.** Temporal evolution of the fractional phase content, as evaluated by CNA.

extension twin was blocked as a result of the size restriction effect. Chakraborty et al. proposed that the fcc structure could be stabilized in Ti films with a thickness much less than 144 nm [40]. Hong et al. reported that the fcc-Ti phase has a thickness of 70 nm or less in hcp-Ti and was divided by persistent slip bands [4]. As the sample size reduced to the nanoscale, as in this case, the stacking faults intersected each other, and the fraction of fcc could reach as high as approximately 24% of the nanopillar.

Gibbs free energy (GFE) is regarded as a criterion for phase transformation. Hcp-Ti is stable structure in bulk state at low temperature, which GFE for hcp structure is  $-466.8 \text{ kJ mol}^{-1}$  smaller than  $-460.5 \text{ kJ mol}^{-1}$  for fcc structure and  $-457.5 \text{ kJ mol}^{-1}$  for bcc structure [41]. However, Xiong et al. [41] found that GFE decreases with the shape factor and increases with the decrease of particle size. As the result, hcp to fcc phase transformation which does not exist in bulk material may occur in nanometer-scale. The prediction is well consistent with experiment result that Ti with the fcc structure is formed at ambient conditions when the grain size is well below 10 nm [15,16].

The results of MD simulations heavily rely on accuracy of empirical or semi-empirical inter-atomic potentials. We have compared EAM [42], MEAM [43] and Finnis–Sinclair many body potentials [33]. The results show that the Finnis–Sinclair many body potential [33] well describes the hcp to fcc phase transition in Ti single-crystal nanopillars during tension loading. No hcp to fcc phase transformation was observed using EAM [42] and MEAM [43] potentials at present simulation conditions.

To study the influence of the nanopillar size and strain rate on the deformation mechanism, the width of nanopillar, which could be effectively simulated, ranged from 2 to 11 nm. The hcp to fcc transformation was observed in this range of sizes with the same deformation mechanism. The nanopillar was also deformed under uniaxial tension at constant strain rates of  $10^7 \text{ s}^{-1}$ – $10^{10} \text{ s}^{-1}$ . The results show that hcp to fcc phase transformation has a strong dependence of strain rate. No hcp to fcc phase transformation was observed above the strain rate of  $10^9 \text{ s}^{-1}$ . Under the higher strain rates, the deformation mechanism is more complex. Further work is needed in the future work.

#### 4. Conclusion

MD simulations of Ti single-crystal nanopillars under uniaxial tension along the (0001) plane show that a rare metastable fcc-Ti phase is formed inside the twinning region of the hcp-Ti phase. The phase transformation is primarily controlled by the partial dislocation slips and stacking faults. The continuous accumulation of the deformation faults eventually leads to the hcp to fcc allotropic phase transformation in the single-crystal Ti nanopillar under tension.

## Acknowledgements

This project was supported by the National Natural Science Foundation of China (51271136, 51071118, 51171140 and 50831004) the 973 Program of China (2010CB631003), and the 111 Project of China (B06025).

## References

- [1] M.F. Aimi, M.P. Rao, N.C. MacDonald, A.S. Zuru, D.P. Bothman, *Nat. Mater.* 3 (2004) 103–105.
- [2] T.N. Pornsin-sirirak, Y.C. Tai, H. Nassef, C.M. Ho, *Sens. Actuators A* 89 (2001) 95–103.
- [3] C. Leyens, M. Peters, *Titanium and Titanium Alloys: Fundamentals and Applications*, Wiley, New York, 2003.
- [4] D.H. Hong, T.W. Lee, S.H. Lim, W.Y. Kim, S.K. Hwang, *Scr. Mater.* 69 (2013) 405–408.
- [5] Cláudio J. DaSilva, José P. Rino, *Comp. Mater. Sci.* 62 (2012) 1–5.
- [6] A.V. Verkhovtsev, A.V. Yakubovich, G.B. Sushko, M. Hanauske, A.V. Solov'yov, *Comp. Mater. Sci.* 76 (2013) 20–26.
- [7] F.E. Wawner, Lawless Jr., K.R. Lawless, *J. Vac. Sci. Technol.* 6 (1969) 588–590.
- [8] A.F. Jankowski, M.A. Wall, *J. Mater. Res.* 9 (1994) 31–38.
- [9] D.V. Heerden, D. Josell, D. Shechtman, *Acta Mater.* 44 (1996) 297–306.
- [10] S.K. Kim, F. Jona, P.M. Marcus, *J. Phys. Condens. Matter* 8 (1996) 25–36.
- [11] P.M. Marcus, F. Jona, *J. Phys. Condens. Matter* 9 (1997) 6241–6246.
- [12] A.A. Saleh, V. Shutthanandan, N.R. Shivaparan, R.J. Smith, T.T. Tran, S.A. Chambers, *Phys. Rev. B* 56 (1997) 9841–9847.
- [13] J.B. Lai, L.J. Chen, C.S. Liu, *Micron* 30 (1999) 205–211.
- [14] Y. Sugawara, N. Shibata, S. Hara, Y. Ikuhara, *J. Mater. Res.* 15 (2000) 2121–2124.
- [15] I. Manna, P.P. Chattopadhyay, P. Nandi, F. Banhart, *J. Appl. Phys.* 93 (2003) 1520–1524.
- [16] P. Chatterjee, S.P. Sengupta, *Phil. Mag.* 81 (2001) 49–60.
- [17] R. Jing, S.X. Liang, C.Y. Liu, M.Z. Ma, X.Y. Zhang, R.P. Liu, *Mater. Sci. Eng. A* 552 (2012) 295–300.
- [18] R. Jing, S.X. Liang, C.Y. Liu, M.Z. Ma, R.P. Liu, *Mater. Sci. Eng. A* 559 (2013) 474–479.
- [19] R. Jing, C.Y. Liu, M.Z. Ma, R.P. Liu, *J. Alloys Comp.* 552 (2013) 202–207.
- [20] V.L. Sliwko, P. Mohn, K. Schwarz, P. Blaha, *J. Phys. Condens. Matter* 8 (1996) 799–815.
- [21] A. Aguayo, G. Murrieta, R. De Coss, *Phys. Rev. B* 65 (2002) 092106.
- [22] Q. Yu, Z.W. Shan, J. Li, X.X. Huang, L. Xiao, J. Sun, E. Ma, *Nature* 463 (2010) 335–338.
- [23] Q. Yu, L. Qi, K. Chen, R.K. Mishra, J. Li, A.M. Minor, *NanoLett.* 12 (2012) 887–892.
- [24] J. Ye, R.K. Mishra, A.K. Sachdev, A.M. Minor, *Scr. Mater.* 64 (2010) 292–295.
- [25] C.M. Byer, B. Li, B. Cao, K.T. Ramesh, *Scr. Mater.* 62 (2010) 536–539.
- [26] E. Lilleodden, *Scr. Mater.* 62 (2010) 532–535.
- [27] G.S. Kim, S. Yi, Y. Huang, E. Lilleodden, *Mater. Res. Soc. Symp. Proc.* 1224 (2010).
- [28] S. Jin, M.J. Burek, N.D. Evans, Z. Jahed, T.Y. Tsui, *Scr. Mater.* 66 (2012) 619–622.
- [29] Q. Sun, Q. Guo, X. Yao, L. Xiao, J.R. Greer, J. Sun, *Scr. Mater.* 65 (2011) 473–476.
- [30] H. Qi, Y. Guo, X. Tang, S. Xu, *Acta Metall. Sin. (Engl. Lett.)* 24 (2011) 487–494.
- [31] J. Ren, Q. Sun, L. Xiao, X. Ding, J. Sun, *Philos. Mag. Lett.* 10 (2013) 583–590.
- [32] S. Plimpton, *J. Comput. Phys.* 117 (1995) 1–19.
- [33] G.J. Ackland, *Phil. Mag. A* 66 (1992) 917–932.
- [34] S. Nosé, *J. Chem. Phys.* 81 (1984) 511–519.
- [35] W.G. Hoover, *Phys. Rev. A* 31 (1985) 1695–1697.
- [36] J. Li, *Modell. Simul. Mater. Sci. Eng.* 11 (2003) 173–177.
- [37] C. Deng, F. Sansoz, *NanoLett.* 9 (2009) 1517–1522.
- [38] J.D. Honeycutt, H.C. Andersen, *J. Phys. Chem.* 91 (1987) 4950–4963.
- [39] G.P. Zheng, Y.M. Wang, M. Li, *Acta Mater.* 53 (2005) 3893–3901.
- [40] J. Chakraborty, K. Kumar, R. Ranjan, S.G. Chowdhury, S.R. Singh, *Acta Mater.* 59 (2011) 2615–2623.
- [41] S. Xiong, W. Qi, B. Huang, M. Wang, Y. Li, *Mater. Chem. Phys.* 120 (2010) 446–451.
- [42] R.R. Zope, Y. Mishin, *Phys. Rev. B* 68 (2003) 024102.
- [43] Y.M. Kim, B.J. Lee, M.I. Baskes, *Phys. Rev. B* 74 (2006) 014101.